9-3-2021

Exploring the structural uniformity and integrity of protonic ceramic thin film electrolyte using wet powder spraying

Wuxiang Feng
Idaho National Laboratory

Wei Wu
Idaho National Laboratory

Congrui Grace Jin
University of Nebraska - Lincoln, cjin5@unl.edu

Meng Zhou
New Mexico State University

Wenjuan Bian
Idaho National Laboratory

See next page for additional authors

Journal of Power Sources Advances 11 (2021) 100067

Contents lists available at ScienceDirect

Journal of Power Sources Advances

journal homepage: www.sciencedirect.com/journal/journal-of-power-sources-advances

Exploring the structural uniformity and integrity of protonic ceramic thin film electrolyte using wet powder spraying

Wuxiang Feng [a,b], Wei Wu [a,**], Congrui Jin [b,c], Meng Zhou [d], Wenjuan Bian [a,d], Wei Tang [a,d], Joshua Y. Gomez [a,d], Richard Boardman [a], Dong Ding [a,*]

[a] Energy & Environmental Science and Technology, Idaho National Laboratory, Idaho Falls, ID, 83401, USA
[b] Department of Mechanical Engineering, Binghamton University, Binghamton, NY, USA
[c] Department of Civil and Environmental Engineering, University of Nebraska–Lincoln, Lincoln, NE, USA
[d] Department of Chemical & Materials Engineering, New Mexico State University, Las Cruses, New Mexico, USA

ARTICLE INFO

Keywords:
Wet powder spraying
Protonic ceramic electrochemical cell
Thin electrolyte film
Steam electrolysis
Fuel cell

ABSTRACT

Thin protonic ceramic electrolyte contributes to lower ohmic resistance and enhances electrochemical performance of protonic ceramic electrochemical cells. However, manufacturing of large-scale thin electrolyte remains a challenge. Wet powder spraying is an attractive technique to deposit <10 μm thin electrolyte when advanced atomizing techniques and optimized spraying process are integrated. Here ultrasonic atomization is integrated in the wet powder spray technique to reduce the thickness of electrolyte. Moreover, a parametric study is conducted to optimize the wet powder spray process to deposit uniform and crack-free electrolyte film. It is illustrated that tuning of solid loading rates and spray passes can affect the morphology of the as-sprayed electrolyte film, enabling the structural compactness of the sintered electrolyte layer. To maintain chemical stability of the electrolyte layer during sintering, effect of sintering temperature is further investigated to produce a physically thin, structurally dense, and chemically homogeneous electrolyte layer. The protonic ceramic electrochemical cells fabricated with optimized spraying and sintering parameters demonstrate excellent performance under both fuel cell and electrolysis modes. In addition, the cells exhibit remarkable structural integrity during redox and long-term stability tests.

1. Introduction

Protonic ceramic electrochemical cells (PCECs) have attracted a significant amount of interest from research communities for several decades due to their lower operating temperature compared with oxygen-ion conducting ceramic electrochemical cells (OCECs). The reduced operating temperatures mitigates many problems such as slow start-up, fast degradation of cell/stack performance, the burden of design, and the cost of thermal insulation required by high temperatures [1,2]. Yttrium- and ytterbium-doped barium-zirconium-cerate (BZCYYb), is one of the most widely studied proton-conducting electrolyte because of its high bulk proton conductivity and greatly improved chemical stability compared to its counterparts [3–7]. It is also a promising material for PCECs operated by hydrocarbon fuel due to its high tolerance to hydrogen sulfide and resistance to carbon accumulation [8–10]. Broader applications are also possible to produce high-value products [11,12].

A thin electrolyte layer with low ohmic resistance is anticipated to promote the electrochemical performance of PCECs. However, the applicability of PCECs with a thin electrolyte is questionable due to their lower-than-predicted performance and difficulties with scaling up the cell fabrication [13–16]. Recently, Ann and Lee et al. demonstrated a 5 × 5 cm^2 PCEC with excellent power density (1.3 W cm^{-2}), which was enabled by employing advanced fabrication techniques and an optimized sintering process [17].

Currently, a thin electrolyte layer can be deposited by either sintering-free techniques or sintering-engaged techniques. Sintering-free techniques include thermal spray [18] and gas phase deposition technologies [19,20] that do not involve high-temperature sintering. The sintering-free techniques are capable of fabricating electrolyte layers with thicknesses in the nanoscale [21]. However, their cost and efficiency of large-scale production are incomparable to

* Corresponding author.
** Corresponding author.
E-mail addresses: wei.wu@inl.gov (W. Wu), dong.ding@inl.gov (D. Ding).

https://doi.org/10.1016/j.powera.2021.100067
Received 5 July 2021; Received in revised form 20 August 2021; Accepted 22 August 2021
Available online 3 September 2021

sintering-engaged techniques [22]. Sintering-engaged techniques are composed of coating and subsequent sintering. They are more widely used than sintering-free techniques but suffer from i) inaccurate stoichiometric control [9], ii) time- and energy-consuming [23], and iii) relatively high coating thickness. The first two issues can potentially be solved by advanced sintering techniques, such as selective laser sintering [23], spark plasma sintering [24], microwave sintering [25], etc. The third issue of thick electrolyte layers in the range of tens of micrometers is caused by the limitation of wet chemical processing techniques. Conventionally, the electrolyte is deposited by coating techniques such as screen printing [17], tape casting (usually followed by lamination or calendaring) [26–30], wet powder spraying (WPS) [31], electrophoretic deposition [32], spin coating [33], and additive manufacturing (primarily inkjet printing) [34]. Among them, screen printing, tape casting, and WPS (also known as spray coating) are the most widely employed techniques in laboratories and can be easily scaled up for industrial practice [22]. WPS is less popular compared with the other two techniques because it requires more processing parameters, making it more demanding for users [35]. However, it has some unique advantages. Compared with screen printing and tape casting, WPS can potentially deposit thinner electrolyte layers due to lower solid loading of its paint. In addition, the electrolyte thickness can be further decreased by incorporating ultrasonic atomization that generates smaller and uniform droplets [36]. For example, Taillades et al. reported an ultrasonic WPS fabrication process that deposited a 4 μm-thick BZCYYb electrolyte on electrode substrate, which is much thinner than previously reported conventional WPS fabrication processes (10–20 μm) [37]. However, most of the previous works used binder-burnout, organic-free electrode support layers as the substrate. Such substrate is brittle and hence less suitable for mass production. Here a more robust substrate, a green-body electrode support layer, is applied, which can reduce the chance of breakage of substrate during transport and increase final passed yield.

In this study, we report an ultrasonic WPS fabrication process using a green body electrode support layer as the substrate. Spraying and sintering parameters were investigated to obtain a physically thin, structurally dense, and chemically homogeneous electrolyte layer. With this approach, we successfully fabricated a 7 μm thin electrolyte on electrode substrate. The fabricated protonic conducting electrochemical cells demonstrate remarkable performance in both fuel cell and electrolysis modes. Furthermore, the cells show excellent structural integrity during redox and long-term stability tests.

2. Experimental

2.1. Preparation of electrode support

The electrode support layer was prepared using a well-established roll-to-roll manufacturing method [38]. First, NiO (Alfa Aesar) and BZCYYb4411 (in-house via solid-state reaction [39]) were mixed in a jar with organic solvents (ethanol and toluene), a dispersant (fish oil, The Tape Casting Warehouse, USA), an organic binder (polyvinyl butyral, The Tape Casting Warehouse, USA), and a plasticizer (butyl benzyl phthalate, The Tape Casting Warehouse, USA) by ball milling for 48 h to obtain a homogeneous slurry. The exact formulation is detailed in Table 1. The obtained slurry was degassed with agitation at the vapor pressure of the organic solvents to remove air bubbles. Subsequently, the slip was tape cast into a wet green tape using a casting machine (TTC-1200, The Tape Casting Warehouse, USA). The tape was dried on a heated bed for 4 h to remove the solvent. Three pieces of green tapes were cut from the dried tape and laminated with a hot press (4130, Carver, USA) into a 1 mm-thick green tape, which served as the electrode support layer.

Table 1
Formulas of electrode slurry and WPS paint.

Chemical	Percentage in electrode slurry (wt.%)	Percentage in WPS paint (wt.%)
NiO	37.7	N/A
BZCYYb4411	25.1	12.2
Fish oil	0.4	0.1
Ethanol	13.6	81.1
Toluene	13.6	4.5
Butyl benzyl phthalate	4.0	0.9
Polyvinyl butyral	5.7	1.3

2.2. Cell fabrication with wet powder sprayed electrolyte

An electrolyte paint (see Table 1 for formulation) was prepared following a similar procedure as the electrode slurry except a 10-min high-energy ball milling (8000D Mixer/Mill, SPEX, USA) was used for mixing. The paint was deposited on the electrode support layer using an ultrasonic spray system (Exactacoat, Sono-Tek, USA) equipped with an AccuMist nozzle. The paint was placed in a syringe pump connected by tubing to the atomizing nozzle. The tip of the ultrasonic atomizing nozzle was actuated at a frequency of 120 kHz with a generator power of 1.2 W. Compressed air was used as the shaping gas at a working pressure of 1 atm to control the shape of the spray coating beam, and the hotplate was set to 70 °C. The spray gun was aligned vertically to the substrate at a distance of 10 cm. The solid loading rates varied from 2.4×10^{-4} to 9.6×10^{-4} g/s, which was controlled through the syringe pump. A rectangular pattern integrated with the PathMaster software was employed as the spray path. The number of layers coated on the substrate varied between 2 and 8 layers, depending on the solid loading rate, to produce electrolytes with the same thickness. Fig. 1 describes the PCEC fabrication procedure with the integrated WPS technique.

After spraying the electrolyte paint, the green tapes were cut to a target size, followed by binder burn-out and sintering in BZCYYb powder bed with additional 10 wt% BaCO3 added, as described by Babilo et al. [40], at 1450–1550 °C for 5 h with a heating rate of 2 °C/min to form the half cell. $PrNi_{0.5}Co_{0.5}O_{3-\delta}$ (PNC), a triple conducting ($H^+/O^{2-}/e^-$) material, was used as the cathode or steam electrode. The PNC slurry was painted on the electrolyte via screen printing and sintered at 950 °C for 5 h in ambient air to form the complete cell, as described in our previous work [41]. For this work, we prepared 1 inch-diameter button cells with an effective area of 3.1 cm^2 to evaluate their electrochemical performance.

2.3. Characterization

The morphology and cross-sections of the PCECs were observed using an optical microscope (Zeiss Axioscope 5 MAT) and a field emission scanning electron microscope (SEM) (FEI QUENTA FEG 650). Silver paste and wire were used for current collection. The cell was sealed on one end of an alumina support tube using Ceramabond 552 adhesive (Aremco Products). The seal was set in ambient air overnight, followed by curing at 93 °C for 2 h and 260 °C for 2 h. The assembly was subsequently heated up to the target temperature with a ramping rate of 3 °C/min. Afterward, the hydrogen electrode side was reduced in pure H_2 gas at a flow rate of 60 sccm. After reduction, air (100 sccm) fed through a bubbler containing distilled water kept at 50 °C was introduced into the steam electrode to obtain 12% steam partial pressure. The electrochemical test was carried out with a Solartron 1400 electrochemical workstation to collect electrochemical performance data, including current-voltage characteristic curves, impedance spectra, redox stability, and electrolysis stability. The ohmic resistance and polarization resistance of the cell was determined from the electrochemical impedance spectra. After performance measurements, the cell was cooled down to ambient temperature at a cooling rate of 1 °C/min.

In a typical redox cycle, the cell was run at 1) open circuit for 1 h, 2) 1.3 V for 2 h, 3) open circuit for 1 h. The gas composition during these

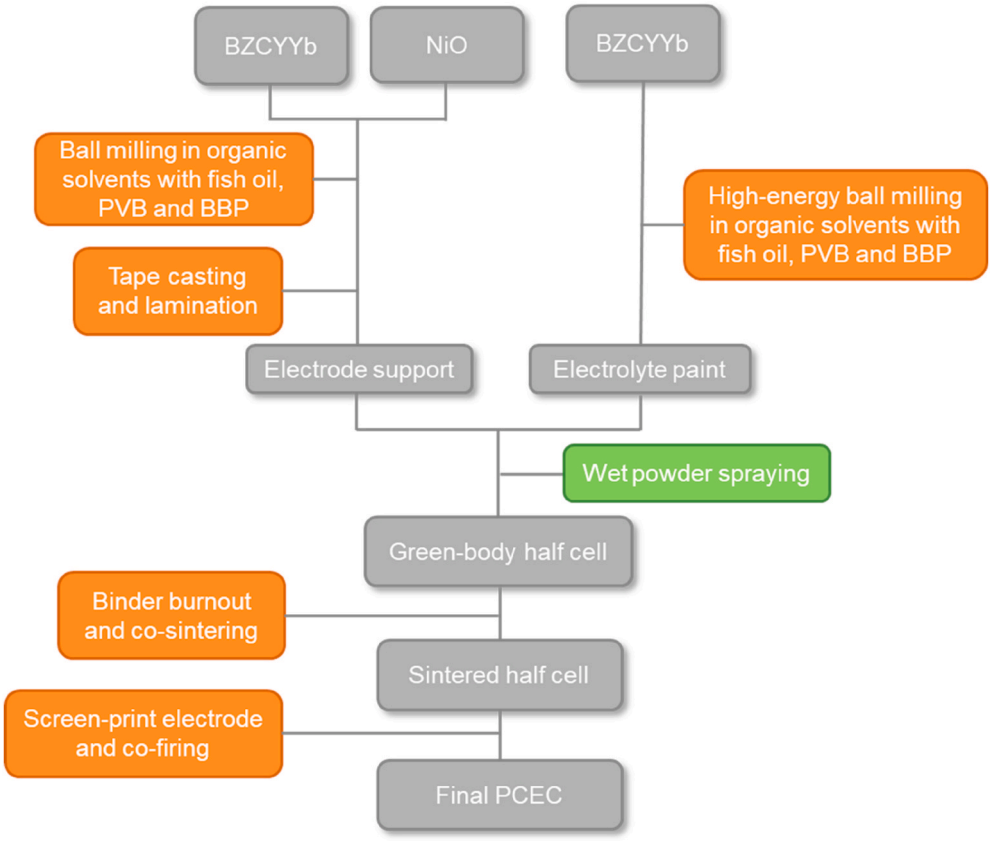

Fig. 1. Procedure of PCEC fabrication with integrated WPS technique.

three steps were 60 sccm H_2 at hydrogen electrode side and 12% steam +78% air (100 sccm) at steam electrode side. Subsequently, the gas at hydrogen electrode side was changed to 60 sccm Ar for 5 min, followed by changing to 60 sccm air for 55 min to oxidize the hydrogen electrode. After oxidation, the hydrogen side was fed with 60 sccm Ar for 5 min and then 60 sccm H_2 for 30 min to reduce the hydrogen electrode. A total of six redox cycles were performed during the redox stability test.

3. Results and discussion

3.1. Optimization of solid loading rate and spray pass

A well-deposited electrolyte layer depends on the paint formulation as well as the processing parameters of the spray process. To optimize the electrolyte morphology, electrolyte layers were prepared with three solid loading rates ranging from 2.4×10^{-4} g/s to 9.6×10^{-4} g/s. Spray passes were controlled to vary with the solid loading rate (listed in Table 2) to fabricate cells with electrolytes of the same thickness. Fig. 2 shows optical microscope images of the as-sprayed electrolyte surfaces and SEM images of the sintered electrolyte surfaces. Cell A has a relatively rough electrolyte surface which is resulted by "orange peel effect" known in the spray-paint industry [42], while cell B and cell C have smoother surfaces. The cause of the "orange peel effect" in this case is that the drying of deposited layer was too fast. To be more specific, the paint first goes through atomizing nozzle and become paint droplets. The droplets strike on substrate, which forms a film containing numerous paint circles. The paint in these circles needs to go through flowing, coalescence, and leveling-down to grow into a uniform film [43]. Due to the drying is too fast, the as-sprayed film on cell A do not have enough time to go through these processes to grow into a uniform film.

Table 2
The solid loading rate and spray passes of cell samples.

Cell	A	B	C	D	E
Solid loading rate (g/s)	2.4×10^{-4}	4.8×10^{-4}	9.6×10^{-4}	4.8×10^{-4}	4.8×10^{-4}
Spray pass	8	4	2	2	8

After sintering, ridges and hollows still existed on the electrolyte surface of cell A, along with fractures possibly caused by uneven shrinkage of the electrolyte during sintering, as shown in Fig. 2(a). The electrolyte surface of cell B had negligible grooves and the most leveled surface among the three cells as shown in Fig. 2(b). For cell C, although it had a smooth and crack-free surface after paint deposition, significant cracks generated on its surface after sintering as shown in Fig. 2(c). A similar phenomenon was observed by Zhou et al. [44]. They brought up an explanation based on the theory of pore shrinkage in powder packing proposed by Kingery and Francois [45]. The theory predicts that a critical pore coordination number (P_c) and pore coordination number (P) exist. If $\eta < 1$ ($\eta = P/P_c$), the pore will shrink. On the contrary, if $\eta > 1$, a pore in the packing does not shrink and may grow [45,46]. To examine if this theory applies to the phenomenon we observed, we inspected cell B and cell C after binder-burnout at 920 °C, as shown in Fig. 3. It illustrated that the distribution of ceramic powders was more uniform in cell B, while large voids and cracks were present in cell C. Hence, cell C had a pore coordination number P that may be greater than the critical coordination number P_c, resulting in a defective electrolyte after sintering [47]. Given that cell B and cell C had different solid loading rates, the higher solid loading rate applied to cell C might be the cause for the formation of cracks. We assume a higher solid loading rate may stimulate the transport of electrolyte particles in the wet film via the coffee ring effect [48,49] and form less uniform electrolyte powder packing containing inter-agglomerate porosity with $\eta > 1$.

As a result, 4.8×10^{-4} g/s was chosen as the solid loading rate for

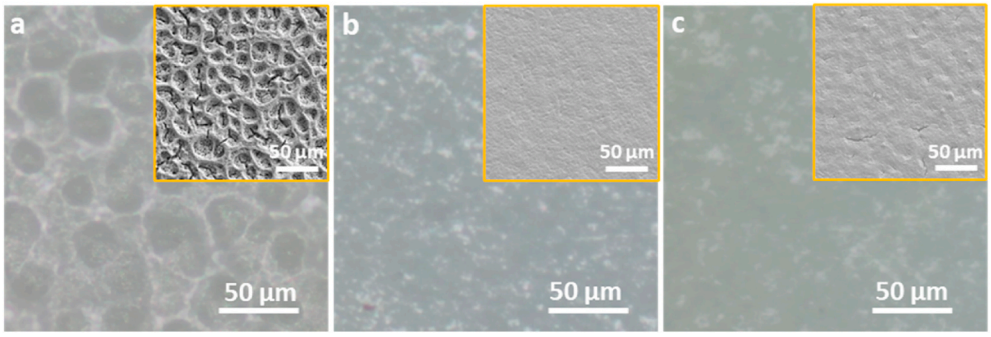

Fig. 2. Optical microscopic images of as-sprayed electrolyte surface and SEM images of sintered electrolyte surface (upper right corners) of (a) cell A, (b) cell B, and (c) cell C.

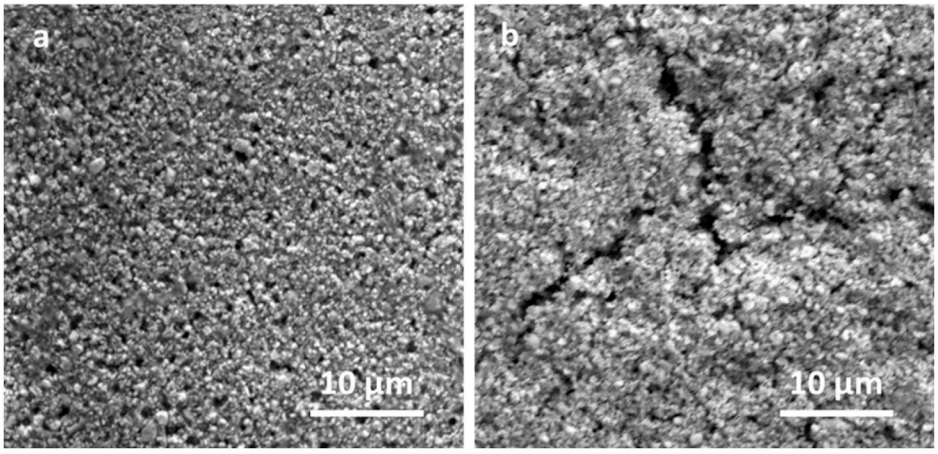

Fig. 3. SEM images of electrolyte surface with a solid loading rate of (a) 4.8×10^{-4} g/s and (b) 9.6×10^{-4} g/s after binder-burnout at 920 °C. The cell C in (b) with electrolyte sprayed at higher solid loading rate might have a higher inter-agglomerate porosity with $\eta>1$, resulting in growth of pores during sintering process.

WPS. To investigate the effect of spray pass on thickness and compactness of electrolyte, we prepared cell D and cell E at same solid loading rate of 4.8×10^{-4} g/s as cell B but with different spray passes, as shown in Table 2. The surface and cross-sectional SEM images of cell B, cell D and cell E are shown in Fig. S1. The figures show that the electrolyte of cell D has significant pores which do not exist on that of cell B and cell E. Electrochemical performance tests were performed on these cells and the results are shown in Supporting Information (Fig. S1). The test showed that only the cells with electrolyte thickness of 7.1 μm (cell B) and 10.8 μm (cell E) have stable OCV at above 1 V, suggesting the 4 μm-thick electrolyte (cell D) is unable to separate fuel from oxygen due to the existence of open pores. The cell B has a higher electrochemical performance compared with cell E due to a lower ohmic resistance brought by its thinner electrolyte.

3.2. Optimization of sintering temperature

The densification of the electrolyte in the BZCYYb/NiO-BZCYYb bilayer is largely attributed to an internal supply of a small but adequate amount of transient phases from the NiO-BZCYYb anode and a larger shrinkage of the anode than of the electrolyte [17]. We prepared multiple cell B sintered at 1450, 1500, and 1550 °C. The SEM images of cell B sintered at different temperatures are shown in Fig. 4(a)–(c). At 1450 °C, open pores were observed on the electrolyte surface and cross-section, making the electrolyte unable to separate fuel from air. When the sintering temperature reached 1500 °C, most open pores were eliminated due to shrinkage and densification, and grain size increased from ~5 μm to ~10 μm. When the sintering temperature reached 1550 °C, grain size changed to ~18 μm while electrolyte thickness did not significantly change compared to the cell sintered at 1500 °C. In addition, impurities were observed on the electrolyte surface which did not exist on other cells.

The distribution of elements on the surface of the cells sintered at 1550 °C was examined by energy dispersive X-ray spectroscopy (EDX). Fig. 4(d) illustrates that areas containing impurities had a higher content of Y and Yb, a lower content of Ba and Ce, and no Ni. This indicates that the temperature at 1550 °C facilitates the disintegration of the perovskite structure and formation of a Y- and Yb-rich oxide phase, which could potentially debilitate the protonic conductivity. The same phenomenon was observed by Han et al. [50] and Babilo et al. [40]. The reason that Y- and Yb-oxide phase did not incorporate into the perovskite phase at 1550 °C is yet to be investigated. Quantitative determination of the phase boundary might be an interesting topic in the future. Electrochemical performance tests were conducted on these cells and demonstrated in Supporting Information as Fig. S2. The results showed significant decrease in peak power density and increase in ohmic and polarization resistance of the cell sintered at 1550 °C compared with the cell sintered at 1500 °C, implying non-stoichiometry of BZCYYb electrolyte caused by higher sintering temperatures.

3.3. Electrochemical performance evaluation

The electrochemical performance of cell B sintered at 1500 °C was measured at different temperature ranging from 500 to 600 °C. Fig. 5(a) and Fig. 5(b) show the current-voltage curves at fuel cell and electrolysis mode, respectively. An OCV of 1.07 V was observed close to the theoretical voltage value of 1.086 V [51] at 600 °C, indicating that the sprayed BZCYYb electrolyte was gas-tight and no leak from the ceramic

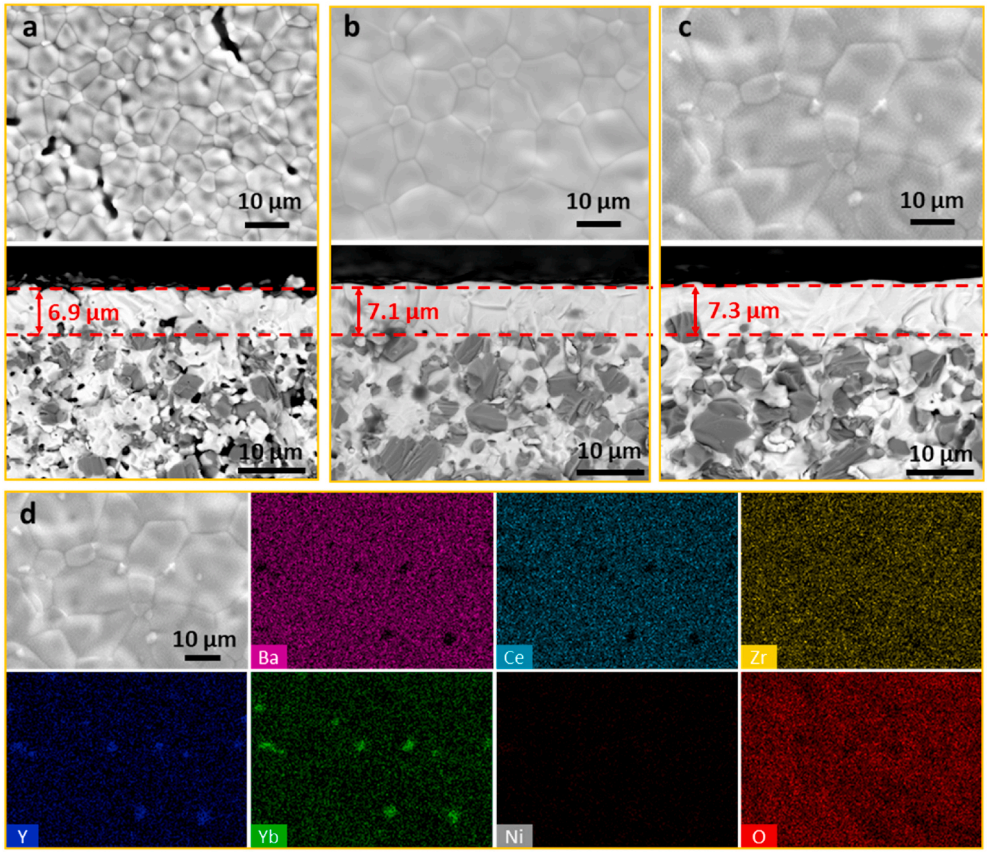

Fig. 4. SEM images of the surface and the cross-sections of cells sintered at (a) 1450 °C, (b) 1500 °C and (c) 1550 °C, and (d) EDX maps of a sprayed cell sintered at 1550 °C for Ba, Ce, Zr, Y, Yb, Ni and O.

seal. The results further confirmed that the 7 μm-thick BZCYYb electrolyte was dense and pinhole-free. In addition, the cell demonstrated remarkable power densities of 732 mW cm^{-2} (600 °C), 602 mW cm^{-2} (550 °C), and 497 mW cm^{-2} (500 °C) under fuel cell mode, and current densities of 820 mA cm^{-2} (600 °C), 527 mA cm^{-2} (550 °C), and 240 mA cm^{-2} (500 °C) at 1.3 V under electrolysis mode. The performance exceeds previously reported cells with WPS sprayed electrolyte as shown in Table 3.

As durability is one of the most important engineering properties of PCECs, it was assessed by two tests. Redox cycling, which is common under practical operation, is known to be unfavorable to cell durability as nickel oxidation leads to a ~40% volume increase relative to elemental nickel, and redox cycling is associated with redistribution of the nickel metal phase [52]. A thin electrolyte needs to be structurally flaw-free and mechanically strong to withstand the mechanical and thermal stress caused by redox cycling. Here a redox stability test was first conducted to evaluate the robustness of our cells. As shown in Fig. 5 (c), the cell remained a stable OCV of 1.05 V after going through six redox cycles. Minor degradation in OCV (~0.03 V in 35 h) was detected over redox cycling process, while significant degradation in current was observed at 1.3 V during the initial three cycles. According to the impedance spectra of each cycle shown in Fig. S3, the degradation was mainly attributed to growth of polarization resistance. The increase of polarization resistance in first three cycles is more significant than the rest of cycles. This may be attributed to the variation in the hydrogen and steam electrodes (both bulk electrode and electrode/electrolyte interface). The insignificant growth of ohmic and polarization resistance in last two cycles aligns with the insignificant degradation in both OCV and current density in Fig. S3. These results imply that the cell remain satisfactory integrity after six redox cycles.

In addition, we conducted a long-term stability test at a constant voltage of 1.3 V under electrolysis mode. As shown in Fig. 5(d), decent stability was observed without significant degradation (only 0.42%) after approximately 200 h at a 12% steam concentration. The cell's physical integrity was unchanged after the test, and no fractures or delamination were detected via SEM, as shown in Fig. S4.

Table 3 compares the performance of our fabricated cell with the cells in previous works. Currently, most of previous works employed a binder-burnout electrode support layer as the substrate in which ceramic powders were weakly bonded, leading to the weak mechanical strength of the substrate. Such substrates require extra caution during transport from a furnace to a spray coater and vice versa. In addition, the use of the binder-burnout electrode support layer also required an additional cooling down and ramping up process, instead of binder burnout directly followed by sintering, which greatly shortens processing time. Our work proved the feasibility of using a green-body electrode support layer as a substrate and demonstrated excellent performance enabled by a thin electrolyte fabricated by an optimized ultrasonic WPS technique.

4. Conclusions

This study demonstrates an ultrasonic WPS fabrication process aiming to fabricate a thin electrolyte layer for PCECs. A more robust green-body electrode support layer is utilized as the substrate instead of a more commonly used binder-burnout one, which is more friendly for handling and simplifies the sintering process. The effect of solid loading rate and spray pass are studied to optimize the as-sprayed electrolyte film. Additionally, the effect of sintering temperature is studied to enhance the chemical homogeneity of the sintered electrolyte. Finally, PCECs at a solid loading rate of 4.8×10^{-4} g/s with 4 spray passes and sintered at 1500 °C yields a uniform 7 μm-thick electrolyte, enabling

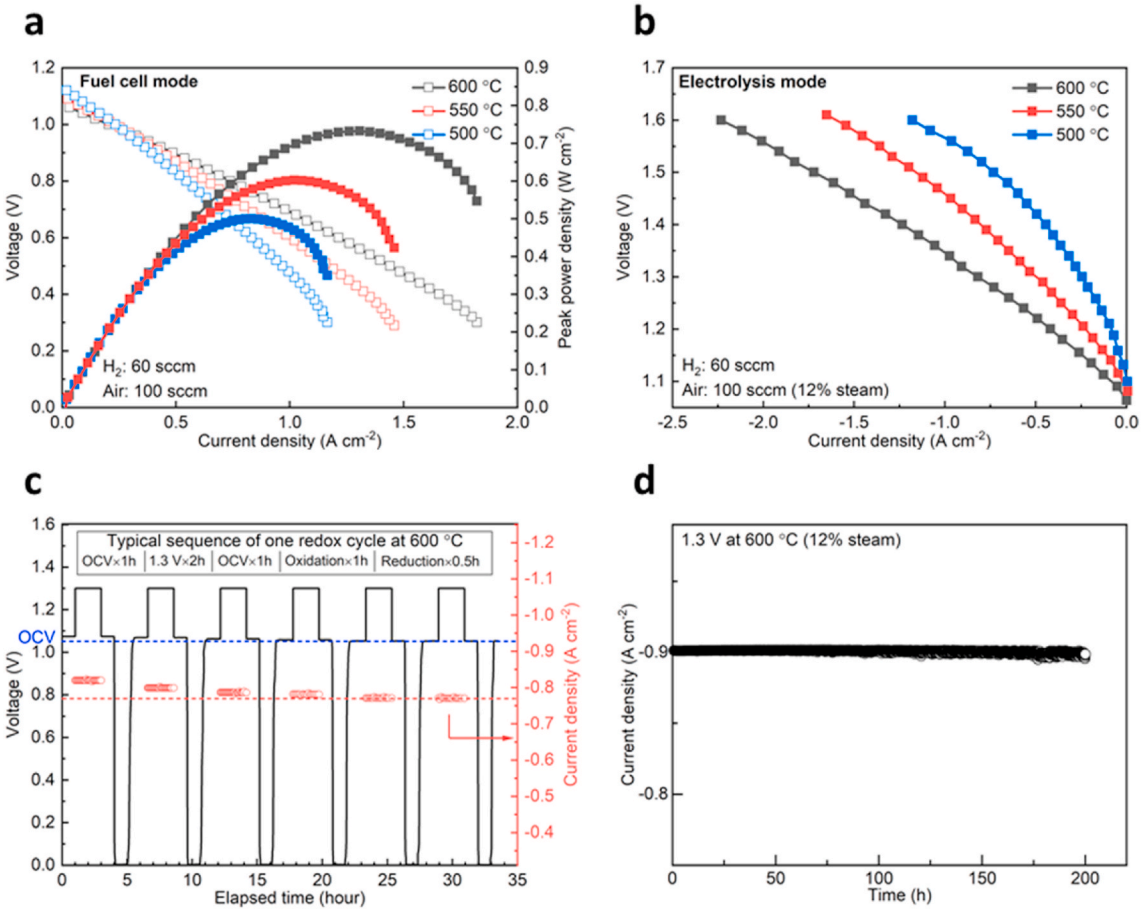

Fig. 5. (a) Electrochemical performance at fuel cell mode of a cell B sintered at 1500 °C measured at different temperatures; (b) Electrochemical performance at electrolysis of cell B sintered at 1500 °C measured at different temperatures; (c) Redox-stability test at 600 °C of cell B sintered at 1500 °C; (d) Long-term test of cell B sintered at 1500 °C under electrolysis mode at 1.3 V and 600 °C.

Table 3
PCECs and SOFCs with electrolyte layers deposited by WPS technique.

Type	Year	Atomizer	Substrate	Electrolyte	thickness (μm)	MPD (mW cm^{-2})	R_{ohmic} (Ω cm^2)	Reference
PCEC	2021	Ultrasonic	Green body	BZCYYb4411	7	732 (at 600 °C)	0.196	This study
	2017	Pressurized	Binder-burnout	BCZY712	17	177 (at 600 °C)	0.68	[53]
	2016	Pressurized	Binder-burnout	BCZY712	18	362 (at 650 °C)	0.28	[54]
	2016	Ultrasonic	Binder-burnout	BCZYYb7111	4	418 (at 600 °C)	0.3	[37]
	2013	Pressurized	Binder-burnout	BCZY622	10–15	493 (at 600 °C)	0.46 (total)	[55]
SOFC	2014	Pressurized	Mylar film	YSZ	15–20	220 (at 700 °C)	N/A	[56]
	2010	Ultrasonic	Binder-burnout	YSZ	33	50 (at 700 °C)	N/A	[57]
	2008	Pressurized	Binder-burnout	YSZ	15	700 (at 750 °C)	0.05	[58]
	2008	Pressurized	Binder-burnout	YSZ	10–20	276 (at 750 °C)	0.5	[44]
	2006	Pressurized	Binder-burnout	YSZ	10	346 (at 700 °C)	0.4	[59]

excellent electrochemical performance in both fuel cell (peak power density of 732 mW cm^{-2} at 600 °C) and electrolysis (current density of 820 mA cm^{-2} at 1.3 V and 600 °C) modes. The cells also showed remarkable structural integrity during long-term and redox stability tests. Overall, this work demonstrated a WPS technique that has great potential for mass manufacturing of PCECs featuring a thin (<10 μm) electrolyte.

Declaration of competing interest

☒ The authors declare that they have no known competing financial interests or personal relationships that could have appeared to influence the work reported in this paper.

Acknowledgements

This work is supported by the U.S. Department of Energy (USDOE), Office of Energy Efficiency and Renewable Energy (EERE), Hydrogen and Fuel Cell Technologies Office (HFTO), Technology Acceleration under DOE Idaho Operations Office under contract DE-AC07-05ID14517. C. J would like to acknowledge a subcontract from Idaho National Laboratory.

Appendix A. Supplementary data

Supplementary data to this article can be found online at https://doi.org/10.1016/j.powera.2021.100067.

References

[1] E.D. Wachsman, K.T. Lee, Lowering the temperature of solid oxide fuel cells, Science 334 (6058) (2011) 935–939, https://doi.org/10.1126/science.1204090.

[2] D. Ding, et al., Enhancing SOFC cathode performance by surface modification through infiltration, Energy Environ. Sci. 7 (2) (2014) 552–575, https://doi.org/10.1039/C3EE42926A.

[3] S. Choi, et al., Exceptional power density and stability at intermediate temperatures in protonic ceramic fuel cells, Nat. Energy 3 (3) (2018) 202–210, https://doi.org/10.1038/s41560-017-0085-9.

[4] W. Wu, et al., 3D self-architectured steam electrode enabled efficient and durable hydrogen production in a proton-conducting solid oxide electrolysis cell at temperatures lower than 600 °C, Adv. Sci. 5 (11) (2018) 1800360, https://doi.org/10.1002/advs.201800360.

[5] Y. Zhang, et al., Basic properties of proton conductor BaZr0.1Ce0.7Y0.1Yb0.1O3-δ (BZCYYb) material, Asia Pac. J. Chem. Eng. 14 (4) (2019) e2322, https://doi.org/10.1002/apj.2322.

[6] Bian, W., et al., Regulation of cathode mass and charge transfer by structural 3D engineering for protonic ceramic fuel cell at 400 °C. Adv. Funct. Mater.. n/a(n/a): p. 2102907, https://doi.org/https://doi.org/10.1002/adfm.202102907.

[7] C.Y. Regalado Vera, et al., A mini-review on proton conduction of BaZrO3-based perovskite electrolytes, J. Phys.: Energy 3 (3) (2021), 032019, https://doi.org/10.1088/2515-7655/ac12ab.

[8] L. Yang, et al., Enhanced sulfur and coking tolerance of a mixed ion conductor for SOFCs: BaZr0.1Ce0.7Y0.2–xYbxO3–δ, Science 326 (5949) (2009) 126–129, https://doi.org/10.1126/science.1174811.

[9] A. VahidMohammadi, Z. Cheng, Fundamentals of synthesis, sintering issues, and chemical stability of BaZr 0.1 Ce 0.7 Y 0.1 Yb 0.1 O 3-δ proton conducting electrolyte for SOFCs, J. Electrochem. Soc. 162 (2015) 803–811, https://doi.org/10.1149/2.0021508jes.

[10] C. Duan, et al., Highly durable, coking and sulfur tolerant, fuel-flexible protonic ceramic fuel cells, Nature 557 (7704) (2018) 217–222, https://doi.org/10.1038/s41586-018-0082-6.

[11] D. Ding, et al., A novel low-thermal-budget approach for the co-production of ethylene and hydrogen via the electrochemical non-oxidative deprotonation of ethane, Energy Environ. Sci. 11 (7) (2018) 1710–1716, https://doi.org/10.1039/c8ee00645h.

[12] M. Li, et al., Switching of metal–oxygen hybridization for selective CO2 electrohydrogenation under mild temperature and pressure, Nat. Catal. 4 (4) (2021) 274–283, https://doi.org/10.1038/s41929-021-00590-5.

[13] S.H. Nien, et al., Preparation of BaZr0.1Ce0.7Y0.2O3–δ based solid oxide fuel cells with anode functional layers by tape casting, Fuel Cell. 11 (2) (2011) 178–183, https://doi.org/10.1002/fuce.201000147.

[14] N.T.Q. Nguyen, H.H. Yoon, Preparation and evaluation of BaZr0.1Ce0.7Y0.1Yb0.1O3−δ (BZCYYb) electrolyte and BZCYYb-based solid oxide fuel cells, J. Power Sources 231 (2013) 213–218, https://doi.org/10.1016/j.jpowsour.2013.01.011.

[15] W. Sun, et al., An easily sintered, chemically stable, barium zirconate-based proton conductor for high-performance proton-conducting solid oxide fuel cells, Adv. Funct. Mater. 24 (36) (2014) 5695–5702, https://doi.org/10.1002/adfm.201401478.

[16] Z. Shi, W. Sun, W. Liu, Synthesis and characterization of BaZr0.3Ce0.5Y0.2−xYbxO3−δ proton conductor for solid oxide fuel cells, J. Power Sources 245 (2014) 953–957, https://doi.org/10.1016/j.jpowsour.2013.07.060.

[17] H. An, et al., A 5 × 5 cm2 protonic ceramic fuel cell with a power density of 1.3 W cm–2 at 600 °C, Nat. Energy 3 (10) (2018) 870–875, https://doi.org/10.1038/s41560-018-0230-0.

[18] D. Soysal, et al., Thermal plasma spraying applied on solid oxide fuel cells, J. Therm. Spray Technol. 22 (5) (2013) 588–598, https://doi.org/10.1007/s11666-013-9929-4.

[19] D.Y. Jang, et al., High performance anode-supported solid oxide fuel cells with thin film yttria-stabilized zirconia membrane prepared by aerosol-assisted chemical vapor deposition, J. Electrochem. Soc. 164 (6) (2017) F484–F490, https://doi.org/10.1149/2.0181706jes.

[20] J.W. Son, 15 - metal oxide thin film-based low-temperature-operating solid oxide fuel cell by interface structure control, in: N. Pryds, V. Esposito (Eds.), Metal Oxide-Based Thin Film Structures, Elsevier, 2018, pp. 331–359.

[21] H. Huang, et al., High-performance ultrathin solid oxide fuel cells for low-temperature operation, J. Electrochem. Soc. 154 (1) (2006) B20, https://doi.org/10.1149/1.2372592.

[22] F. Tietz, H.P. Buchkremer, D. Stöver, Components manufacturing for solid oxide fuel cells, Solid State Ionics 152–153 (2002) 373–381, https://doi.org/10.1016/S0167-2738(02)00344-2.

[23] S. Mu, et al., Rapid laser reactive sintering for sustainable and clean preparation of protonic ceramics, ACS Omega 5 (20) (2020) 11637–11642, https://doi.org/10.1021/acsomega.0c00879.

[24] J. Bu, P.G. Jönsson, Z. Zhao, Dense and translucent BaZrxCe0.8−xY0.2O3−δ (x=0.5, 0.6, 0.7) proton conductors prepared by spark plasma sintering, Scripta Mater. 107 (2015) 145–148, https://doi.org/10.1016/j.scriptamat.2015.06.006.

[25] M.A. Janney, C.L. Calhoun, H.D. Kimrey, Microwave sintering of solid oxide fuel cell materials: I, zirconia-8 mol% yttria, J. Am. Ceram. Soc. 75 (2) (1992) 341–346, https://doi.org/10.1111/j.1151-2916.1992.tb08184.x.

[26] W. Wu, et al., In-situ investigation of quantitative contributions of the anode, cathode, and electrolyte to the cell performance in anode-supported planar SOFCs, Adv. Energy Mater. 4 (10) (2014) 1400120, https://doi.org/10.1002/aenm.201400120.

[27] H. Moon, et al., Development of IT-SOFC unit cells with anode-supported thin electrolytes via tape casting and co-firing, Int. J. Hydrogen Energy 33 (6) (2008) 1758–1768, https://doi.org/10.1016/j.ijhydene.2007.12.062.

[28] W. Wu, W. Guan, W. Wang, Contribution of properties of composite cathode and cathode/electrolyte interface to cell performance in a planar solid oxide fuel cell stack, J. Power Sources 279 (2015) 540–548, https://doi.org/10.1016/j.jpowsour.2015.01.060.

[29] H.A. Eltawahni, et al., Tape casting and lamination, in: Reference Module in Materials Science and Materials Engineering, Elsevier, 2019.

[30] W. Wu, et al., Effect of contact method between interconnects and electrodes on area specific resistance in planar solid oxide fuel cells, Fuel Cell. 13 (5) (2013) 743–750, https://doi.org/10.1002/fuce.201300028.

[31] M. Liu, F. Uba, Y. Liu, A high-performance solid oxide fuel cell with a layered electrolyte for reduced temperatures, J. Am. Ceram. Soc. 103 (9) (2020) 5325–5336, https://doi.org/10.1111/jace.17203.

[32] E.G. Kalinina, E.Y. Pikalova, New trends in the development of electrophoretic deposition method in the solid oxide fuel cell technology: theoretical approaches, experimental solutions and development prospects, Russ. Chem. Rev. 88 (12) (2019) 1179–1219, https://doi.org/10.1070/RCR4889.

[33] E.H. Kang, et al., Protonic ceramic fuel cells with slurry-spin coated BaZr0.2Ce0.6Y0.1Yb0.1O3- δ thin-film electrolytes, J. Power Sources 465 (2020) 228254, https://doi.org/10.1016/j.jpowsour.2020.228254.

[34] W. Feng, et al., Manufacturing techniques of thin electrolyte for planar solid oxide electrochemical cells, Electrochem. Soc. Interface 29 (4) (2020) 47, https://doi.org/10.1149/2.F06204IF.

[35] N.H. Menzler, et al., Materials and manufacturing technologies for solid oxide fuel cells, J. Mater. Sci. 45 (12) (2010) 3109–3135, https://doi.org/10.1007/s10853-010-4279-9.

[36] A.H. Lefebvre, Properties of sprays, Part. Part. Syst. Char. 6 (1–4) (1989) 176–186, https://doi.org/10.1002/ppsc.19890060129.

[37] G. Taillades, et al., High performance anode-supported proton ceramic fuel cell elaborated by wet powder spraying, Int. J. Hydrogen Energy 41 (28) (2016) 12330–12336, https://doi.org/10.1016/j.ijhydene.2016.05.094.

[38] H. Ding, W. Wu, D. Ding, Advancement of proton-conducting solid oxide fuel cells and solid oxide electrolysis cells at Idaho national laboratory (INL), ECS Trans. 91 (1) (2019) 1029, https://doi.org/10.1149/09101.1029ecst.

[39] W. Wu, D. Ding, T. He, Development of high performance intermediate temperature proton-conducting solid oxide electrolysis cells, ECS Trans. 80 (9) (2017) 167–173, https://doi.org/10.1149/08009.0167ecst.

[40] P. Babilo, T. Uda, S.M. Haile, Processing of yttrium-doped barium zirconate for high proton conductivity, J. Mater. Res. 22 (5) (2011) 1322–1330, https://doi.org/10.1557/jmr.2007.0163.

[41] H. Ding, et al., Self-sustainable protonic ceramic electrochemical cells using a triple conducting electrode for hydrogen and power production, Nat. Commun. 11 (1) (2020) 1907, https://doi.org/10.1038/s41467-020-15677-z.

[42] J. Konieczny, G. Meyer, Computer rendering and visual detection of orange peel, J. Coating Technol. Res. 9 (3) (2012) 297–307, https://doi.org/10.1007/s11998-011-9378-2.

[43] A. Goldschmidt, H.-J. Streitberger, BASF Handbook on Basics of Coating Technology, 2, Vincentz Network, Hannover, 2007, p. 792.

[44] W. Zhou, et al., Fabrication of an anode-supported yttria-stabilized zirconia thin film for solid-oxide fuel cells via wet powder spraying, J. Power Sources 184 (1) (2008) 229–237, https://doi.org/10.1016/j.jpowsour.2008.06.021.

[45] W.D. Kingery, The sintering of crystalline oxides, I. Interactions between grain boundaries and pores, Sintering Related Phenomena (1967) 471–498.

[46] A.V. Galakhov, Pore coordination number and sintering, Refract. Ind. Ceram. 51 (2) (2010) 83–87, https://doi.org/10.1007/s11148-010-9264-y.

[47] R.K. Bordia, S.-J.L. Kang, E.A. Olevsky, Current understanding and future research directions at the onset of the next century of sintering science and technology, J. Am. Ceram. Soc. 100 (6) (2017) 2314–2352, https://doi.org/10.1111/jace.14919.

[48] H. Hu, R.G. Larson, Marangoni effect reverses coffee-ring depositions, J. Phys. Chem. B 110 (14) (2006) 7090–7094, https://doi.org/10.1021/jp0609232.

[49] T. Carey, et al., Spray-coating thin films on three-dimensional surfaces for a semitransparent capacitive-touch device, ACS Appl. Mater. Interfaces 10 (23) (2018) 19948–19956, https://doi.org/10.1021/acsami.8b02784.

[50] D. Han, et al., Strategy to improve phase compatibility between proton conductive BaZr0.8Y0.2O3−δ and nickel oxide, RSC Adv. 6 (23) (2016) 19288–19297, https://doi.org/10.1039/C5RA26947D.

[51] R.P. O'Hayre, et al., Fuel Cell Fundamentals, third ed. ed., John Wiley & Sons Inc., Hoboken, New Jersey, 2016, p. 1.

[52] M.M. Welander, et al., Operando studies of redox resilience in ALT enhanced NiO-YSZ SOFC anodes, J. Electrochem. Soc. 165 (3) (2018) F152–F157, https://doi.org/10.1149/2.0531803jes.

[53] J. Xiao, et al., Fabrication and characterization of BaZr0.1Ce0.7Y0.2O3−δ based anode supported solid oxide fuel cells by tape casting combined with spray coating, Mater. Lett. 189 (2017) 192–195, https://doi.org/10.1016/j.matlet.2016.10.114.

[54] L. Fan, H. Xie, P.-C. Su, Spray coating of dense proton-conducting BaCe 0.7 Zr 0.1 Y 0.2 O 3 electrolyte for low temperature solid oxide fuel cells, Int. J. Hydrogen Energy 41 (15) (2016) 6516–6525, https://doi.org/10.1016/j.ijhydene.2016.03.001.

[55] Y. Yoo, N. Lim, Performance and stability of proton conducting solid oxide fuel cells based on yttrium-doped barium cerate-zirconate thin-film electrolyte, J. Power Sources 229 (2013) 48–57, https://doi.org/10.1016/j.jpowsour.2012.11.094.

[56] L. Zhang, et al., Preparation of half-cell by bi-layer wet powder spraying and tape casting for anode-supported SOFCs, J. Alloys Compd. 586 (2014) 10–15, https://doi.org/10.1016/j.jallcom.2013.08.186.
[57] A.M. Sukeshini, et al., Investigation of aerosol jet deposition parameters for printing SOFC layers, in: ASME 2010 8th International Conference on Fuel Cell Science, Engineering and Technology, ASMEDC, 2010.
[58] J. Ding, J. Liu, An anode-supported solid oxide fuel cell with spray-coated yttria-stabilized zirconia (YSZ) electrolyte film, Solid State Ionics 179 (21–26) (2008) 1246–1249, https://doi.org/10.1016/j.ssi.2008.01.094.
[59] R. Yan, et al., Thin yttria-stabilized zirconia electrolyte and transition layers fabricated by particle suspension spray, J. Power Sources 164 (2) (2007) 567–571, https://doi.org/10.1016/j.jpowsour.2006.11.060.

Supporting Information

Exploring the structural uniformity and integrity of protonic ceramic thin film electrolyte using wet powder spraying

Wuxiang Feng[1,2], Wei Wu[1*], Congrui Jin[2,3], Meng Zhou[4], Wenjuan Bian[1,4], Wei Tang[1,4], Joshua Y. Gomez[1,4], Richard Boardman[1] and Dong Ding[1*]

[1]Energy & Environmental Science and Technology, Idaho National Laboratory, Idaho Falls, Idaho 83401, USA

[2]Department of Mechanical Engineering, Binghamton University, Binghamton, New York, USA

[3]Department of Civil and Environmental Engineering, University of Nebraska–Lincoln, Lincoln, Nebraska, USA

[4] Department of Chemical & Materials Engineering, New Mexico State University, Las Cruses, New Mexico, USA

*: Corresponding author:

Email: wei.wu@inl.gov (Wei Wu), dong.ding@inl.gov (Dong Ding)

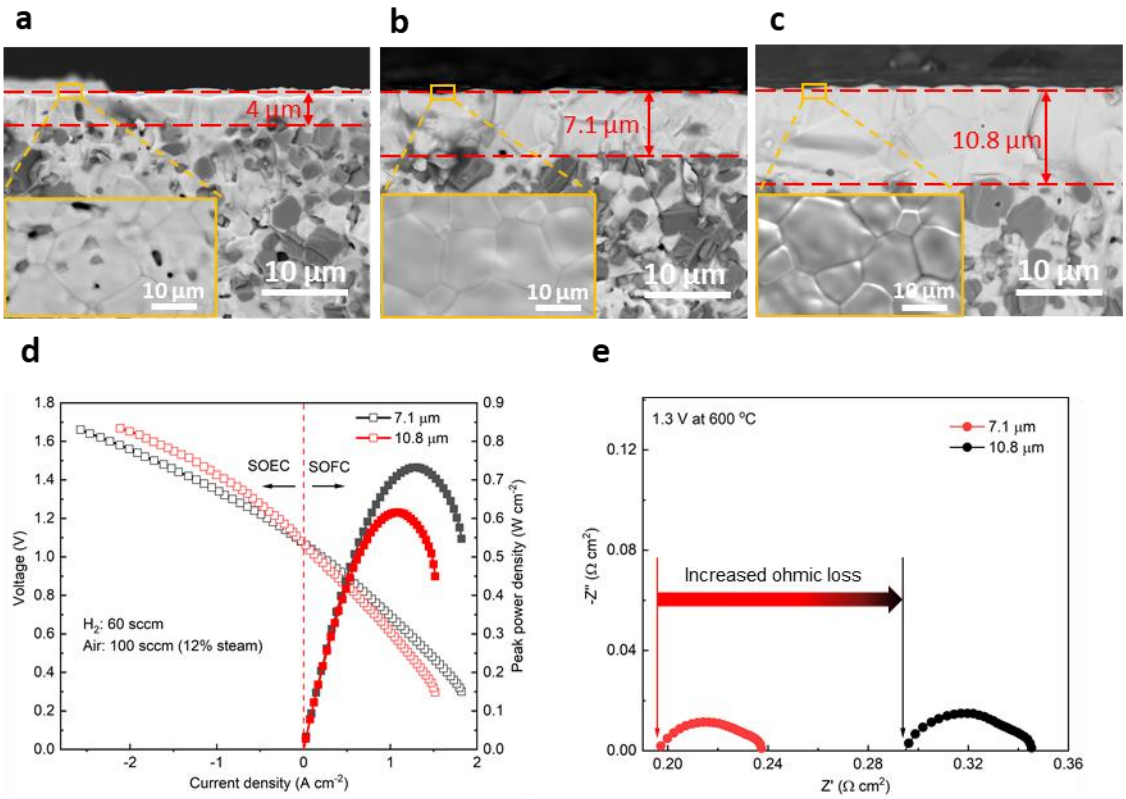

Figure S1. Surface and cross-sectional SEM images of (a) cell D, (b) cell B and (c) cell E after sintering at 1500 °C; (d) I-V and power density of cells with electrolyte thickness of 7.1 μm and 10.8 μm; (e) EIS of cells with electrolyte thickness of 7.1 μm and 10.8 μm.

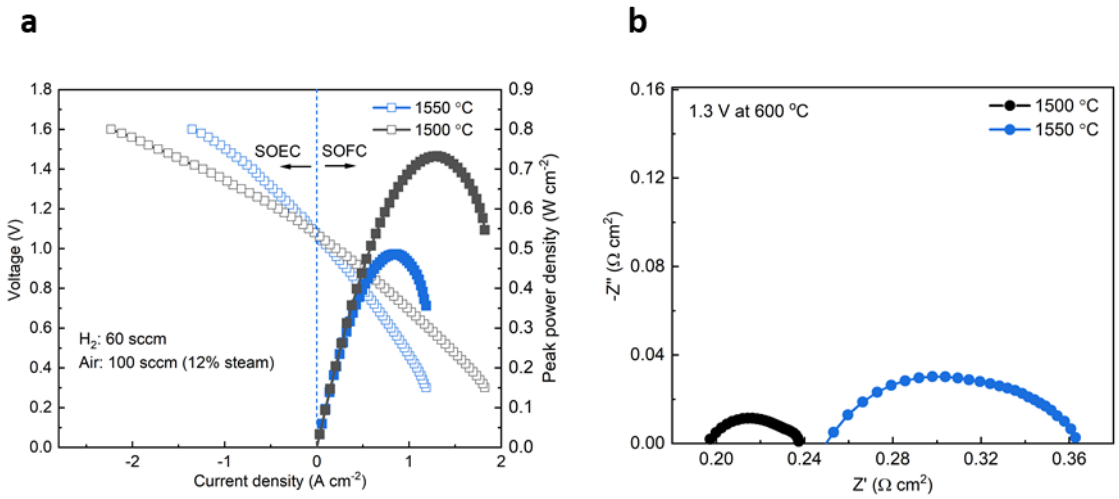

Figure S2. (a) I-V and power density and EIS of cells with electrolyte sintered at 1500 °C and 1550 °C.

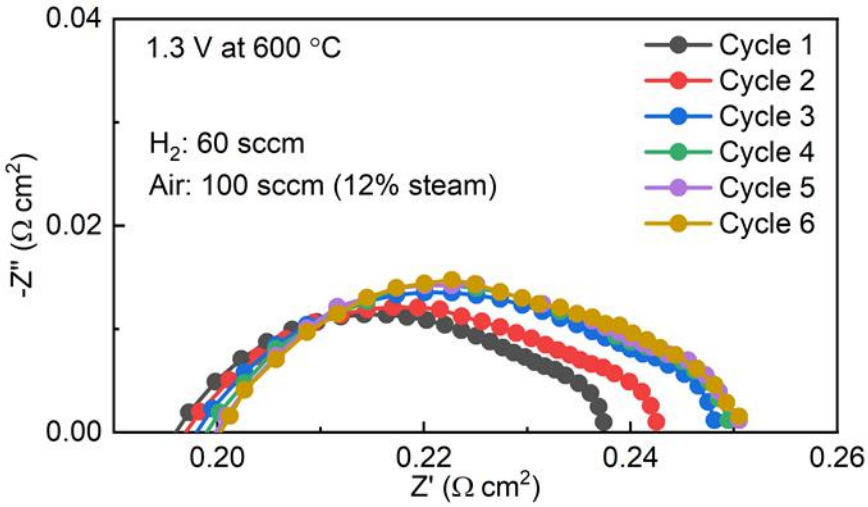

Figure S3. Variation of impedance spectra measured at 1.3 V and 600 ℃

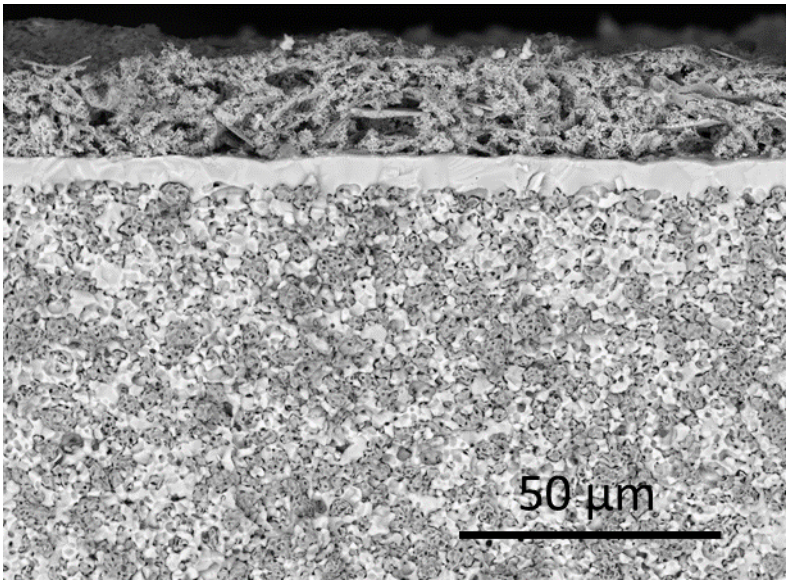

Figure S4. SEM images of cross-section of a sprayed cell sintered at 1500 °C after 200 h long-term stability testing under electrolysis mode at 1.3V and 600 °C.